Type of paper: full-length article (Journal Name – **International Journal of Heat and Mass Transfer**)
Date text written: 05/2019
Date text revised: 07/2019
Number of words in the main text and tables = 6173
Number of figures = 16
Number of tables = 1

Quantifying the impact of rigid interparticle structures on heat transfer in granular materials using networks

Author 1
Wenbin Fei, PhD
Department of Infrastructure Engineering, The University of Melbourne, Parkville, Australia

Author 2
Guillermo A. Narsilio✉, PhD, MSc (Math), MSc (CE), CEng
Department of Infrastructure Engineering, The University of Melbourne, Parkville, Australia

Author 3
Joost H. van der Linden, PhD.
Department of Infrastructure Engineering, The University of Melbourne, Parkville, Australia

Author 4
Mahdi M. Disfani, PhD, MSc, BSc
Department of Infrastructure Engineering, The University of Melbourne, Parkville, Australia

Abstract:

Coordination number can be used to quantify the particle connectivity and deformability of a granular material. However, it is a local feature of particles at the microscale, and the use of an average coordination number does not allow for full characterization of the microstructural variation in the granular material. Mesoscale structures can be used to overcome this limitation: triangular-like structures at the mesoscale tend to be rigid, whereas square-like structures tend to be deformable. However, the effect of these structures on heat transfer has not been studied in deforming granular materials. A better understating of how microstructure variation affects effective thermal conductivity is necessary. This work constructs contact networks representing the granular materials with particles as nodes and linking neighbouring nodes with edges that represent particle contacts. Then, '3-cycles' (i.e., a triangular structure) and 'clustering coefficients' are extracted from the contact network. As contact thermal conductance is vital to heat transfer and affected by particle shape, microscale three-dimensional particle shape descriptors are also calculated. To calculate the effective thermal conductivity of the granular assembly, a thermal network model is established by adding 'near-contact' edges to the contact network and assigning a thermal conductance to each edge. The results show that mesoscale local clustering coefficients can indicate the rigidity of granular materials and, together with particle shape descriptors, can be used to well predict the effective thermal conductivity of granular materials under deformation.

Keywords

Heat transfer; Rigidity; Thermal network model; Microstructure; Deformation.

1 Introduction

Compaction is one of the simplest ways to improve the ground bearing capacity. It also has the potential to enhance the heat transfer of the ground in shallow geothermal energy systems because the interparticle contact areas and the number of interparticle contacts may increase while pore spaces shrink during compaction. Heat transfer in any materials occurs because of conduction, convection and radiation. Since convection is important due to fluid currents [1] and radiation becomes significant when the temperature is greater than 1,000 K [2, 3], conduction usually contributes the most strongly to heat transfer in dry granular materials [1, 4]. The heat conduction depends on the thermal conductivity of solid particles [1], the interparticle contact conductance [1, 5-9] and the structure of particle packings [2, 10]. As the rigidity/deformability of granular materials is related to their microstructures [11], a better understating of how the microstructure variation affects the effective thermal conductivity (λ_{eff}) is necessary.

The coordination number has a strong relationship with mechanical stability [12] and the jamming transition [13, 14] in granular materials. However, the coordination number is a microscale variable describing the connection of an individual particle to others. The often-used average coordination number cannot fully capture the spatial variation of the microstructure of granular materials. An order characteristic can also indicate the packing structure by measuring the rotational symmetry of particles [15]. However, it required complex calculation and was applied to sphere packings in the study. According to rigidity theory, a triangular structure tends to resist more deformation than a quadrilateral structure under an external loading (Fig. 1). However, the effect of interparticle triangular structures on λ_{eff} has not been studied in deforming granular materials.

Complex network theory can quantify the structure of a complex system and it has been successfully applied to represent civil infrastructure systems [16-18]. As granular materials are also complex systems [19], complex network theory has also been used to investigate the mechanical behaviour [11, 20] and pore connectivity [21] in the granular materials. However, it has not been used to study heat transfer in granular materials. A granular material could be simplified as a contact network in which a node is assigned to each particle and an edge is created when two neighbouring particles are in contact. Various mesoscale structural features can be obtained by calculating the number of *n*-cycles using complex network theory [20]. A 'cycle' is a loop that begins and ends at the same node, so 3-cylce is a triangle, 4-cycle is quadrangle and 5-cycle is pentagon. A 3-cycle is the smallest arrangement of particles formed by 3 neighbouring particles in contact [22]. These 3-cycle structures are more persistent and stable than n-cycle of higher orders (n>3) during deformation of granular materials [11]. 3-cycles have a crucial role in rigidity because they can frustrate rotation and provide lateral support to surrounding particles even in three-dimensional (3D) analyses [23, 24]. Rivier (2006) showed that odd circuits (3-cycle is an odd circuit) are sufficient to ensure stability in 3D [23]. Mesoscale clustering coefficients can also be extracted from the contact network to measure the density of 3-cycles (triangles). Compared with the coordination number, which only provides information on a single node, the mesoscale 3-cycle and clustering coefficients have the advantage of containing information about more than one node without comprising the entire network. Hence, investigating the relationship between mesoscale rigidity features and λ_{eff} can potentially improve our knowledge of heat transfer in deforming granular materials.

<Fig. 1 around here>

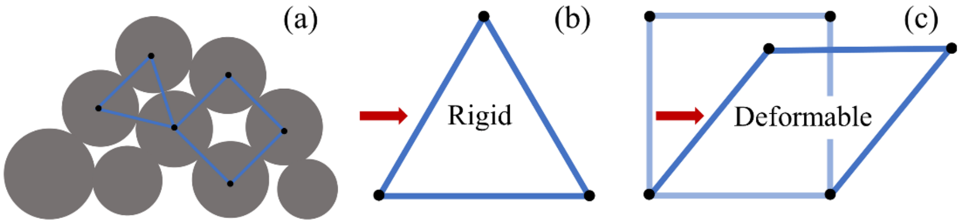

Fig. 1. In representing the structure of a granular material in the network, a triangular structure (a '3-cycle' in complex network theory) is rigid whereas a quadrilateral structure is deformable.

In addition to the microstructure (rigidity) of the packings that can be characterized by the 3-cycle or cluster coefficients, particle contact thermal conductance is also important in the overall heat conduction [25]. In dry materials, the contact conductance is believed to be affected by particle shape [26, 27], as particle shape affects both the contact number and contact area [1, 28]. Therefore, a three-dimensional particle shape descriptor is employed here to study the variation in λ_{eff}.

To extract the '3-cycle' and particle shape descriptors of granular materials, their internal microstructural information should be acquired. High-resolution X-ray computerized tomography (CT) techniques applied to granular materials can generate sequential CT images at a certain interval (resolution) [29-31]. Based on the images, the particle geometrical information and connectivity can be extracted using imaging postprocessing techniques. The geometry of the granular materials can also be reconstructed and numerical simulations can be undertaken to estimate their λ_{eff}. Finite element simulation (FEM) is an available method to compute the λ_{eff} but it is time-consuming because fine meshes are required to discretize the interparticle contacts and the interface between solid and pore phases. It usually overestimates λ_{eff} due to oversmoothing the interparticle contact areas [32, 33] and the lack of consideration of particle surface roughness [32]. Alternatively, network models [34-36] can discretely represent particle packings and calculate the heat transfer through interparticle contacts (real contacts) and small gaps between particles (near-contacts). However, very few thermal network models are available for nonsphere packings. The thermal conductance network model (TCNM) [37] developed by our team extended the application to packings of irregular (i.e., nonspherical) particles.

This article aims to find the relationship between the deformability of granular materials or rigidity and the λ_{eff} of granular materials using network techniques. Five granular materials with different particle shapes were scanned using CT techniques under different loadings. For each material at each level of compaction, four smaller subsamples were selected to (i) construct contact networks to calculate the number of mesoscale 3-cycle and clustering coefficients to characterize the rigidity of granular materials, (ii) construct thermal conductance network models (TCNMs) to calculate λ_{eff}, and (iii) compute the shape descriptors of individual particles. The λ_{eff} calculated from TCNMs were compared to those from FEM and experiments. Then, multiscale parameters were used to analyze the reasons underlying the λ_{eff} variation in deforming materials.

2 Materials

Five granular materials were used in this work. The pictures in the upper row of Fig. 2 show that the selected materials have different particle shapes. The round glass beads were made of silica and have a silver coating. The Ottawa sand was sieved following ASTM standard C778

[38] to achieve particles retained between sieve No. 20 (0.60 mm) and No. 30 (0.85 mm). Particles in both Ottawa sand and Angular sand are mainly made of quartz, but the former are more rounded. Crushed schist A is made of chlorites and the particles in the packings are more irregular than the Angular sand. Crushed schist B has the most irregular particles, which consist of quartz and biotite [39]. Each material was air-pluviated into a cylindrical container with a diameter of 25 mm and a height of 25 mm. This container was equipped with a loading module designed by Afshar et al. [40]. The five materials were scanned under different axial loads corresponding to 0, 2, 6.1 and 10.2 MPa stress levels. The images shown in the bottom row of Fig. 2 are typical cross-section images of the five materials without loading (0 MPa). The voxels with a resolution of 13 μm in them present different grayscale that indicates the density of the mineral. The distinct grayscale in the voxels of the crushed schist CT image results from the corresponding different mineral components. Selecting the resolution of CT images is a trade-off between obtainning fewer grains with higher resolution and more grains with lower resolution. CT images with high resolution could better identify the partial contacts which may be wrongly recognized as a “complete or full contact” between particles [41] otherwise (at lower resolutions) and result in an overestimate [42] of interparticle contact area between irregular grains. The particle size of the five materials is summarized in Table 1.

<Fig. 2 around here>

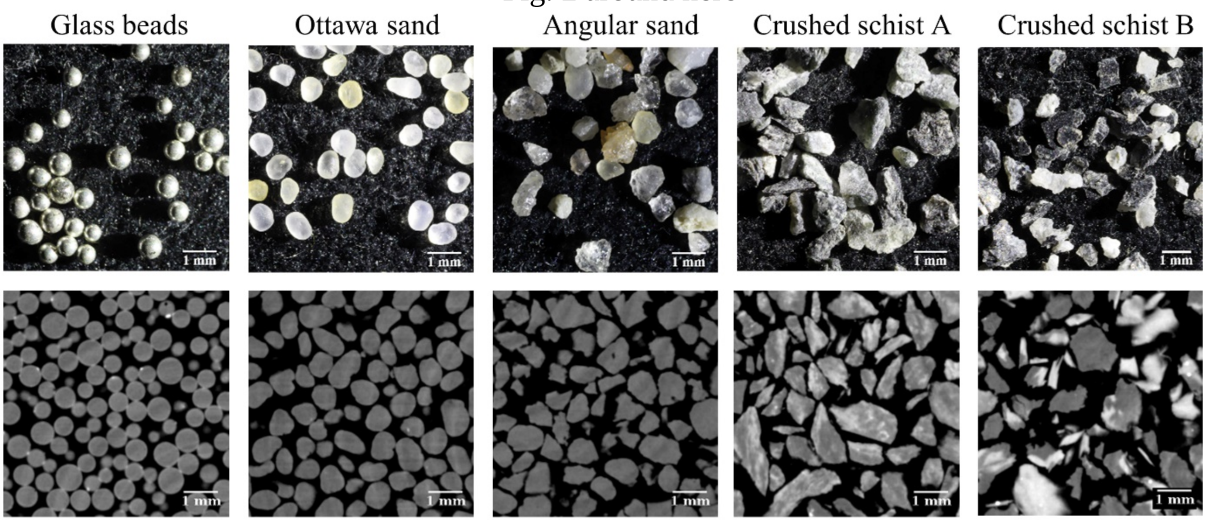

Fig. 2. Five natural sands with different particle shapes. The pictures in the first row were photographed and the images in the second row were scanned with computed tomography.

Table 1 Particle size characteristics of the selected granular materials

Sample	d_{50} (mm)	Particle size range (mm)
Glass beads	0.60	0.50 – 0.70
Ottawa sand	0.73	0.60 – 0.85
Angular sand	0.89	0.60 – 1.18
Crushed schist rock A	0.84	0.50 – 1.18
Crushed schist rock B	0.84	0.50 – 1.18

3 Methods

3.1 Network construction

Two types of networks are constructed in this work. *Contact* networks are constructed to acquire the 3-cycles and cluster coefficients using complex network theory. *Thermal* networks are extensions of the contact networks that also consider near-contacts as edges (Fig. 3) and it can be used to calculate the λ_{eff} by adding thermal conductance at the edges.

As summarized in Fig. 3, a sequence of CT images with a representative element volume is cropped from the scanned sample and the image noise is decreased by using 3D Median filter in Step 1. These images are used to reconstruct the (3D) geometry in which the two phases (solid in black and pore in grey) are segmented with a common multilevel Otsu segmentation method [42-45] implemented in Fiji with automatic parameters selection [46] in Step 2. They do differ for each sample testedTo determine the location of each particle for constructing the networks, the watershed segmentation from MorphoLibJ [47] in Fiji is employed to split connected particles [48] in Step 3. Although Taylor et al. [49] found that the watershed segmentation with a 26 voxel neighbourhood can better capture the boundary of irregular particles, the results usually overestimate the surface (contact) area [50]. Therefore, a 6-voxel neighbourhood was used in this work because it has been shown to render satisfactory results [50].

After the watershed segmentation, each particle is assigned a unique identifier (ID) and its centroid is calculated as the average coordinates of the voxels in the particle. To identify the real interparticle contact and near-contacts, the voxels in each particle are grouped as boundary voxels if they are adjacent to anything other than the voxels in the same particle. A subset of these boundary voxels is identified as interparticle contact voxels if they also border on another particle (and its corresponding boundary voxels). To efficiently identify the near-contacts, watershed segmentation is also applied to the void space (grayscale colours in Fig. 4-left) by first inverting the colour of phases and then following the same steps as with the solid phase watershed segmentation. The particle-pore connection (orange arrows) can be detected if the boundary voxels border on pore space. Then, the particle-pore-particle connections are identified as the location of potential near-contacts. Next, to determine the voxels that form part of a near-contact, cylinders representing gaps between particles or 'gap' cylinders are created for boundary voxels on a particle, as shown in Fig. 4-right, and their lengths $\mathrm{L}_{\mathrm{i}}^{\mathrm{g}}$ are computed as the minimum distance to the boundary voxels on the neighbouring particle. Finally, the gap cylinder(s) will be considered to be in a near-contact if their respective lengths are shorter than a threshold ϵ. The threshold ϵ is selected as half of the mean particle radius after a calibration [37].

< Fig. 3 around here>

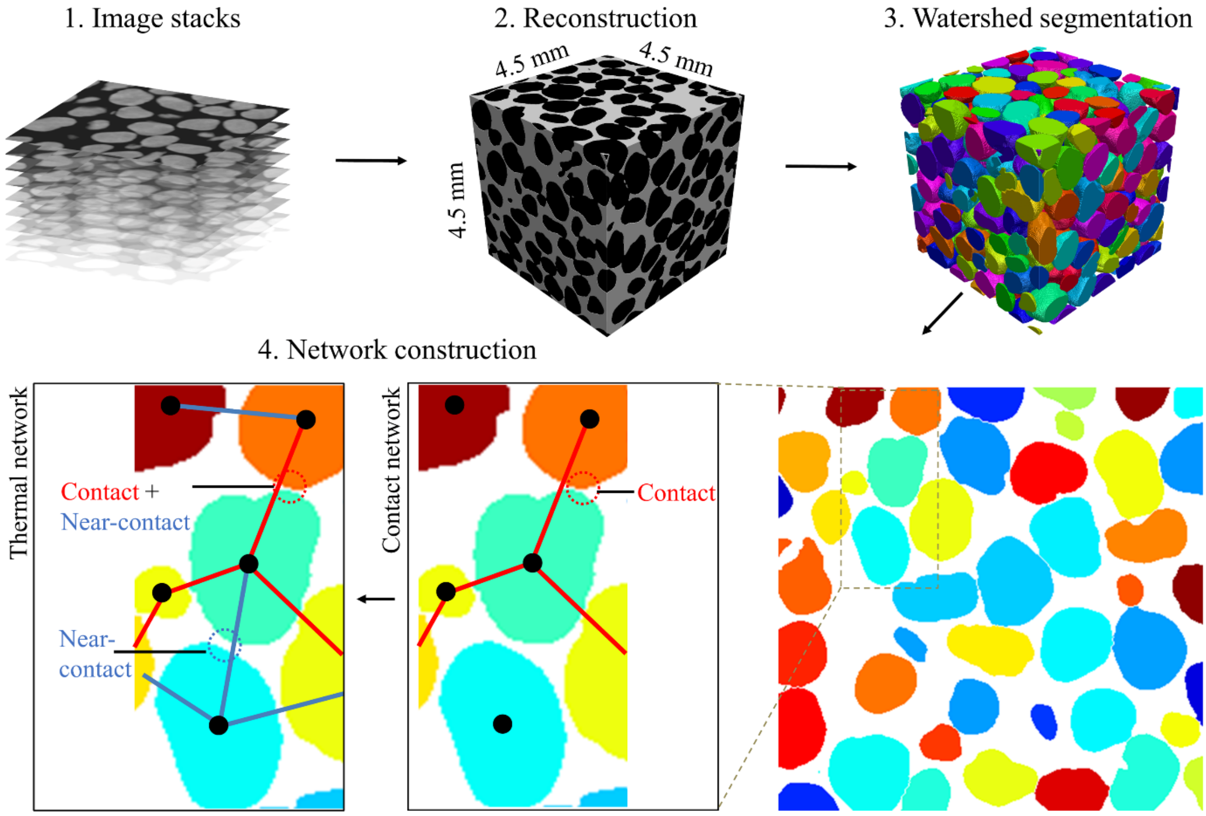

Fig. 3. Procedures to construct a contact network and a thermal network. Contact edges are in red, near-contact edges are in blue.

< Fig. 4 around here>

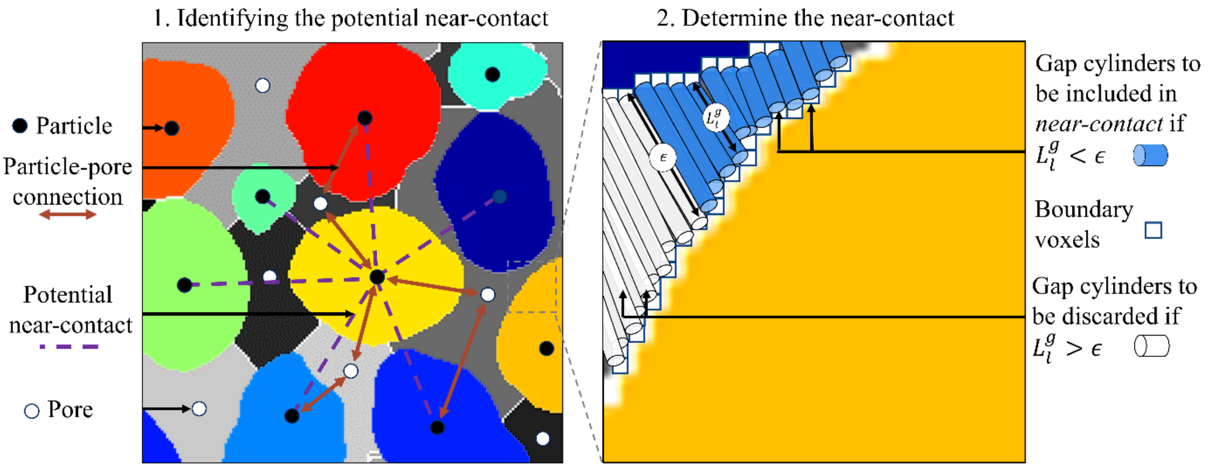

Fig. 4. Identification of near-contacts. ϵ is the threshold length ($D_{50}/4$ in this case) for near-contacts.

3.2 Contact network features

After constructing contact networks, three contact network features (3-cycle, local clustering coefficient and global clustering coefficient) are extracted as rigidity features to indicate the mesoscale structure of granular materials. N_3-cycles is calculated as the number of triangles in the contact network. Local clustering coefficients [51] and global clustering coefficients [20] measure the density of triangles and can be computed using Equations 1 and

2, respectively. The local clustering coefficient, in particular, can quantify the fraction of possible triangles through each node. Clustering coefficients also indicate how fractured or integrated the contact network is. For instance, Fig. 5 (a) is a relatively fractured network that has a higher clustering coefficient than the network in Fig. 5 (b).

$$[G^C]_{LC}\,(\mathrm{i}) = \frac{2T(i)}{N(i)(\mathrm{N}(i)-1)} \tag{1}$$

where T(i) is the number of triangles that pass node i, and N(i) is the degree of node i.

$$G^C{}_{GC} = 3 \cdot \frac{number\ of\ triangles}{number\ of\ connected\ triples} \tag{2}$$

where a triple is a group of three nodes that can contain either three edges (in a 3-cycle) or two edges.

<Fig. 5 around here>

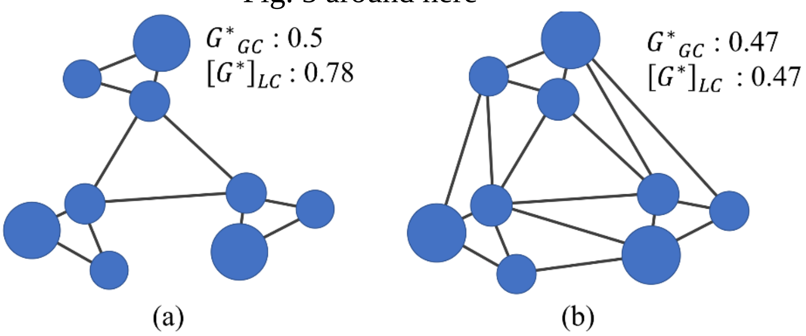

Fig. 5. (a) A fractured network with a local clustering coefficient of 0.78 and global clustering coefficient of 0.5 (b) An integrated network with a local clustering coefficient of 0.47 and global clustering coefficient of 0.47.

3.3 Thermal conductance network model

3.3.1 Thermal conductance calculation

The thermal conductance at the thermal network edges is required to calculate the effective thermal conductivity of granular materials [34]. For a cylinder with cross-sectional area A, length L and thermal conductivity λ, its heat conductance C can be calculated as $C = \lambda A/L$. Hence, equivalent cylinders are used to represent the heat conductance in network edges. These representations were proposed by Batchelor and O'brien [52] for randomly arranged sphere packings and then developed for more general assemblies, as validated by Yun and Evans [34] for spheres and Shapiro et al. [53] for powder packed beds. As heat conducts through solids, real interparticle contacts and near-contacts, three types of equivalent cylinders [37] are considered in this work and summarized in Fig. 6: (i) a particle cylinder with conductance C^p, (ii) a real interparticle contact cylinder $C^{contact}$ and (iii) a near-contact cylinder C^{gap}. The conductances through a 'particle' cylinder and interparticle contact cylinder can be computed using Equations 3 and 4, respectively,

$$\mathrm{C^p} = \lambda_s \frac{A^p}{L^p} = \lambda_s \frac{\chi V^P / L^P}{L^P} \tag{3}$$

where λ_s represents the thermal conductivity of the solid and the void phase. L^P is the distance between the centroid of a particle and its corresponding contact. L^P is equal to the particle radius for a spherical particle. The particle cylinder area A^P is derived as $\chi V^P / L^P$. Here, V^P is the particle volume and χ is a model coefficient that can be computed as $1/N(i)$ where $N(i)$ is the coordination number of particle i (i.e., the degree of node i in contact network).

$$\mathrm{C}^{contact} = \lambda_s \frac{\kappa A^C}{L^C} = \lambda_s \frac{\kappa \sum_{i,j,k} A^v_{i,j,k}}{3\, L^v} \tag{4}$$

where A^C is the interparticle contact area computed as the sum of the area of contact voxel $\sum_{i,j,k} A^v_{(i,j,k)}$ and L^v is the length of a voxel However, interparticle contact is essentially a combination of contact points because of the particle surface roughness [54]. The results of Askari et al. [54] show that a 25% overestimation of λ_{eff} may occur due to neglecting the roughness. Thus, κ is set as 0.75 in our work. L^C is the length of the interparticle contact cylinder, assumed to be $3 \cdot L^v$ [37] refer to the work of Bauer and Schlunder [55] that was validated by Shapiro et al. [53].

Interparticle contact is usually over-smoothed during the threshold segmentation, as illustrated in Fig. 7, where the voxels partially filled with solid and void are incorrectly identified as a contact. The over-smoothing of the contact area results in a higher λ_{eff} in simulation [32, 33]. Since the partially filled voxels have specific grayscales, a penalty coefficient τ [37] is introduced to correct the area of partially filled voxels as:

$$A^v_{(i,j,k)} = \left(\frac{g_{(i,j,k)}}{g^{contact}_{max}}\right)^{\tau} L_v^2 \tag{5}$$

where $g_{(i,j,k)} \in (0{,}255)$ is the gray value of each voxel (i, j, k) at the interparticle contact and the $g^{contact}_{max}$ is the largest value among them. The power of τ is used to vary the severity of the penalty and is set as 10 [37] after calibrating the λ_{eff} of sphere packings using the results of an existing thermal network for sphere packings [34].

Near-contact cylinders are generated based on the near-contacts identified in Fig. 4. Then, the conductance at near-contact cylinders C^{gap} can be calculated as:

$$\mathrm{C}^{gap} = \sum_l C^g_l = \lambda_v (L^v)^2 \sum_l \frac{1}{L^g_l} \tag{6}$$

where λ_v represents the thermal conductivity of the void phase and L^g_l is the length of the near-contact cylinder.

<Fig. 6 around here>

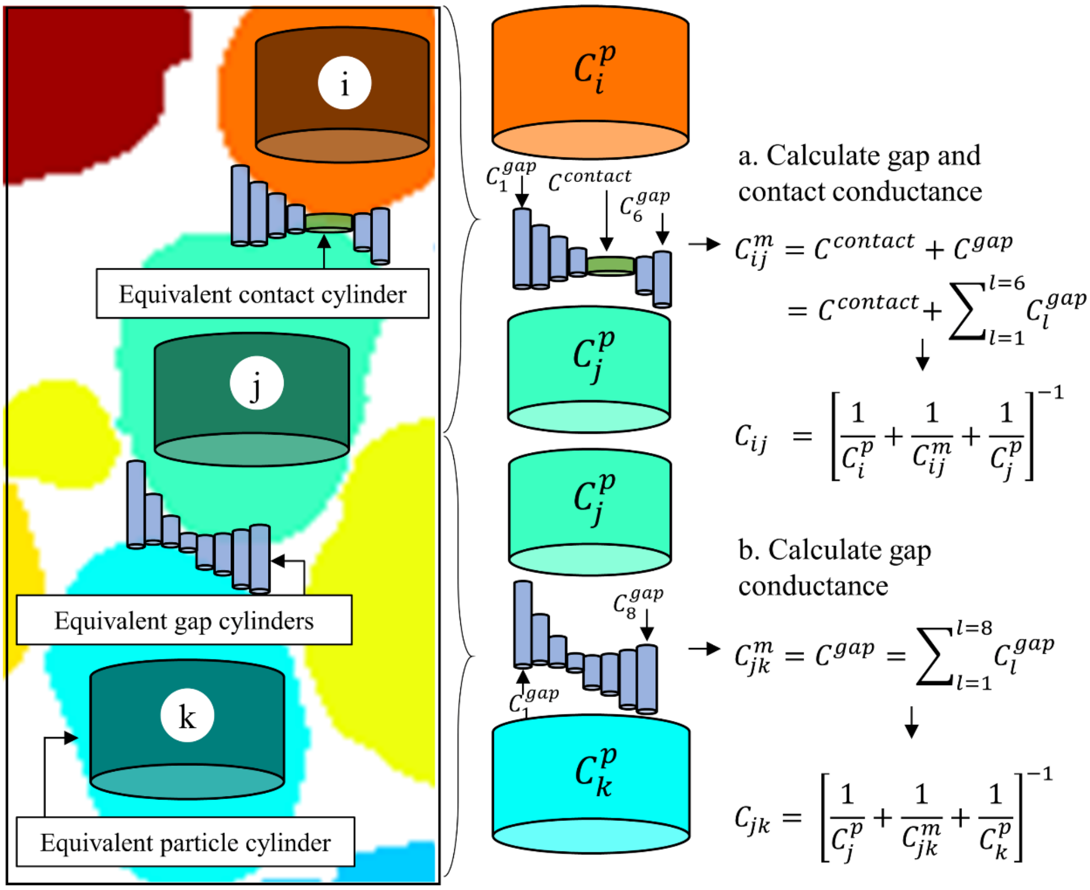

Fig. 6. Computation of thermal conductance in the thermal conductance network (TCNM).

<Fig. 7 around here>

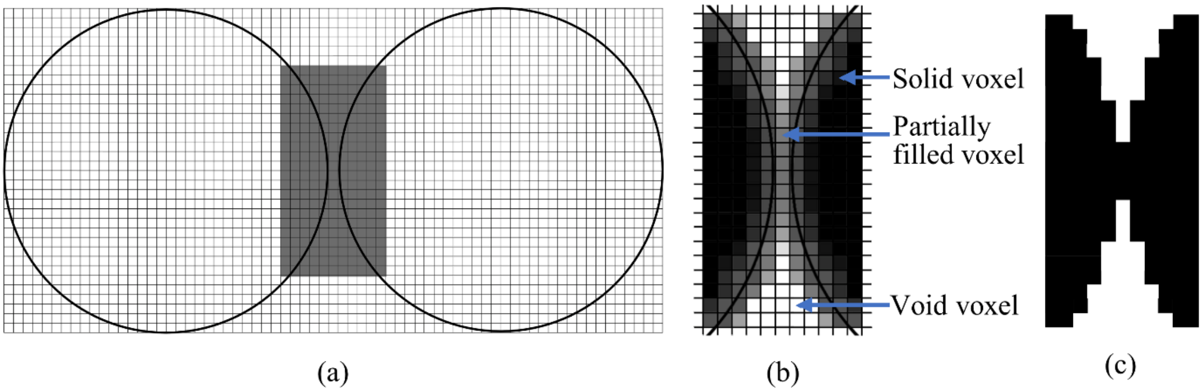

Fig. 7. Over-smoothing of CT images after threshold segmentation: (a) Two discs with a 1-pixel gap; (b) a small gap in grayscale; (c) over-smoothing in the contact after threshold segmentation (after [42]).

3.3.2 Effective thermal conductivity calculation

To calculate the λ_{eff} of dry granular materials by solely considering heat conduction, the heat flux Q_{ij} of an edge connecting nodes i and j is solved by importing the computed thermal conductances to Fourier's law (Equation 7) as part of the open-source Python library OpenPNM [56]. As this study focuses on the structure variation beyond the mineralogy, the thermal conductivity of the solid was fixed at 3 W/(m K) [1, 34, 57] and the thermal conductivity of the air filled in the void space is 0.025 W/(m K). The boundary temperatures at the top and bottom nodes are 293 K and 292 K, respectively. The heat flux is calculated as:

$$\sum_{i \to j} Q_{ij} = \sum_{i \to j} C_{ij}(T_i - T_j) \tag{7}$$

where C_{ij} is the conductance of the interparticle contact of the near-contact conductance and T_i and T_j are the temperatures at nodes i and j.

After calculating the local heat flux Q_{ij} at each edge, the total heat flux in a typical cross-sectional plane perpendicular to the heat transfer direction can be used in Equation 8 to compute the λ_{eff} of the sample. A simulation result by TCNM is shown in Fig. 8.

$$\lambda_{\mathrm{eff}} = \frac{\frac{1}{A}\int_A Q_z\, dA}{(T_a - T_b)/L} = \frac{\frac{1}{A}\sum Q_{ij}}{(T_a - T_b)/L} \tag{8}$$

<Fig. 8 around here>

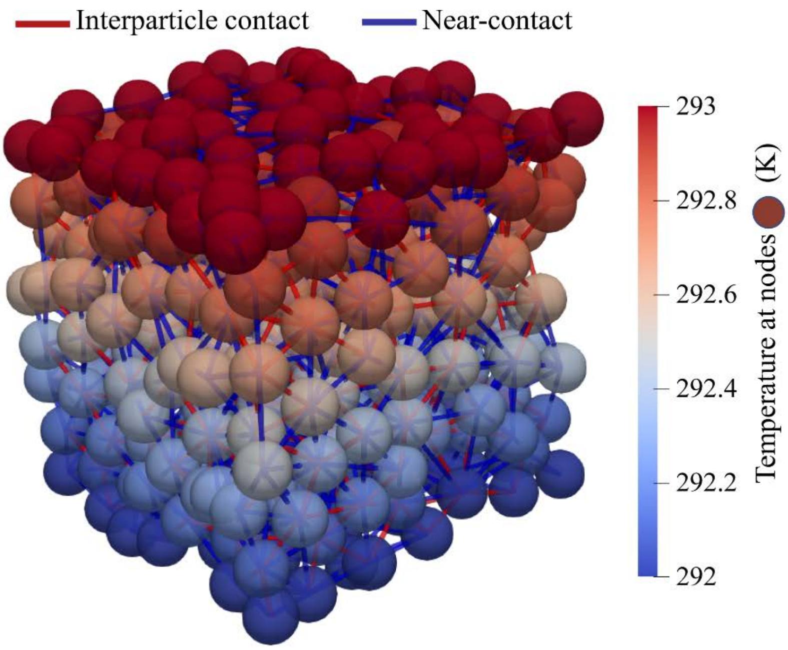

Fig. 8. TCNM simulation results showing the temperature of each node. From this network system, it is easy to see paths of heat transfer: interparticle contacts are shown in red and the near-contacts are blue.

3.4 Finite element simulation and laboratory measurement

To validate the heat transfer simulation by TCNM, finite element simulation and thermal needle testing were also used to measure the λ_{eff} of the granular materials.

3.4.1 Finite element simulation

We follow the framework introduced by Narsilio et al. [58] for fluid flow and its adaption for heat transfer at the particle scale [32, 37, 59]. For each sample, CT image stacks were imported to Simpleware ScanIP [60] to reconstruct the 3d microgeometry, segment the solid and void (Step 2 in Fig. 3), and generate meshes that are transferred to the finite element software COMSOL Multiphysics [61] for heat transfer simulation. *Fig.* 9 shows the mesh of

Ottawa sand, the mesh size and sample size were decided after a sensitivity analysis. The input thermal conductivity of air and solid grains are same as that in TCNM (solids at 3 $\mathrm{W/(m\,K)}$, air at 0.025 $\mathrm{W/(m\,K)}$). Similar to the simulation process in TCNM, the local temperature is first calculated by solving the governing balance energy equations for a system with thermal insulation on all sides and a small temperature cdifferential between the top and bottom boundaries (*Fig.* 9). The local heat flux density Q_z is estimated from the local temperature field using Fourier's law. Finally, the integrated format $\frac{1}{A}\int_A Q_z\, dA$ in Equation 8 is used to determine the effective thermal conductivity of the sample. Additional details on this procedure can be found in papers [32, 37, 58].

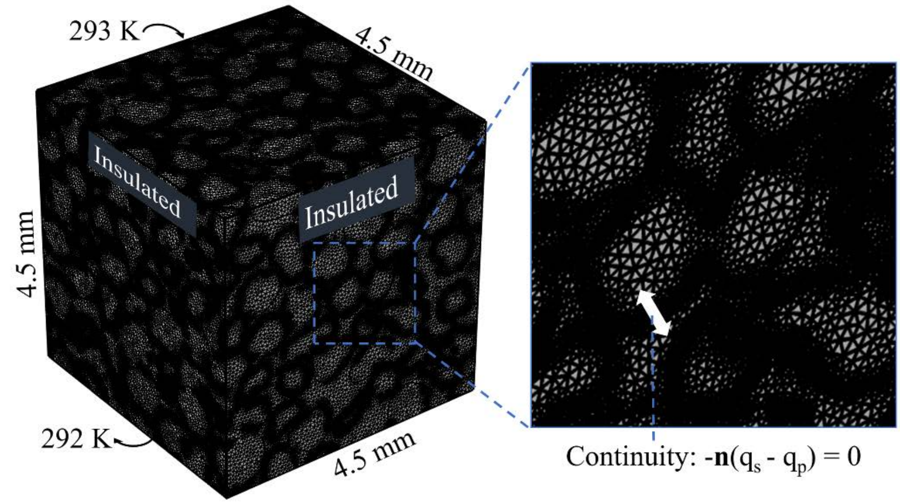

Fig. 9. The finite elements and boundary condition used for simulating the heat transfer in Ottawa sand without loading.

3.4.2 Laboratory measurement

A 100-mm long thermal needle probe with a diameter of 2.4 mm was used to measure the λ_{eff} in the laboratory. The diameter of the needle was selected to be larger than the particle diameter to maximize the contacts between particles and the thermal needle probe. The granular materials were air-pluviated into a PVC cylinder with a diameter of 50 mm and a height of 120 mm. We followed ASTM standard D5334-14 [62] to measure the thermal conductivity of the air-pluviated materials, achieving good accuracy at $\pm 10\%$ for $0.2 - 4$ W $/$(mK) [63].

3.5 Particle shape descriptors

Sphericity (S) and roundness (R) are two indicators that describe particle shape and can be calculated using Equations 9 [47] and 10 [64], respectively.

$$S = \frac{36\pi V^2}{\mathrm{SA}^3} \tag{9}$$

where V is the particle volume and SA is the particle surface area.

$$R = \frac{\sum r_i/N}{r_{max-in}} \tag{10}$$

where r_i is the radius of a particle corner, N is the total number of corners and $r_{\mathrm{max-in}}$ is the radius of the maximum inscribed sphere in the particle.

To calculate the sphericity and roundness of each particle automatically based on CT images, an in-house program has been developed [28]. Since the connected particles were separated in Step 3 (Fig. 3), the individual particles can be extracted from the samples. The surface mesh of the extracted particles from CT images have tooth-saw patterns (Fig. 10), which may overestimate the particle volume and particle surface area, so the Taubin smoothing algorithm [65] is applied to achieve a smooth particle surface (Fig. 10). Since the smooth particle surface is composed of triangles, the sum of each triangle surface area is the particle surface area. Similarly, a tetrahedron is constructed for each triangle by considering the centre of the particle, and the sum of the volume of all the tetrahedrons is the particle volume.

Identifying the corners in each particle is required and their radii are used to calculate the roundness using Equation 10. The maximum curvature of each vertex is first computed by quadratically fitting a microsurface using its ring adjacent vertices. Next, a quadratic polynomial equation can be obtained and the principal curvatures can be calculated by solving Hassian matrix [66] which created with coefficients in the equation. Then, corners are identified if the absolute value of the reciprocal of the curvature is smaller than r_{max-in}, the radius of the maximum inscribed sphere in the particle, and the reciprocal is selected as the radius of the corner r_i.

<Fig. 10 around here>

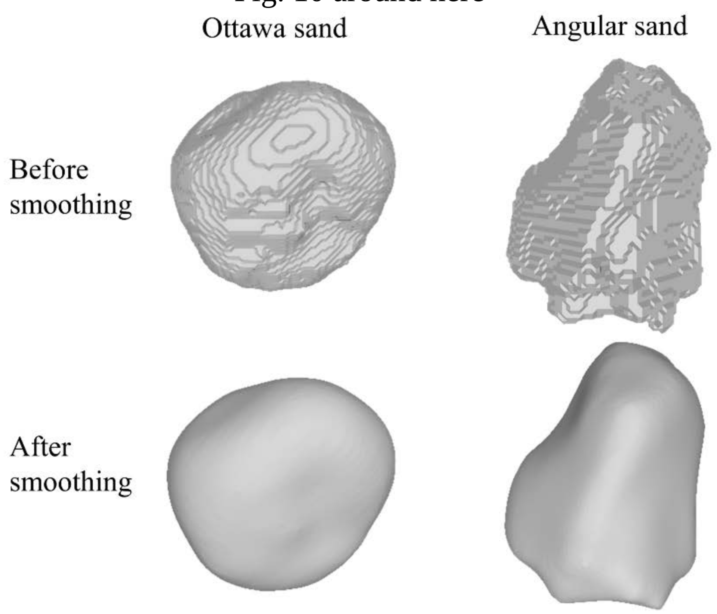

Fig. 10. The Taubin smoothing algorithm is used to transform the particles with a tooth-saw surface to a smooth surface.

4 Results and discussion

4.1 Effective thermal conductivity comparisons

For each material shown in Fig. 2 under no pressure, four subsamples with a dimension of 4.5 by 4.5 by 4.5 mm from random locations within the sample were selected to check the homogeneity of the sample. Their λ_{eff} were calculated by both FEM and TCNM, as shown in Fig. 11. Experimental measurements from the literature [32, 34] and our laboratory are also included. The porosity of the experimental results is the mean value of the four subsamples in FEM and TCNM.

<Fig. 11 around here>

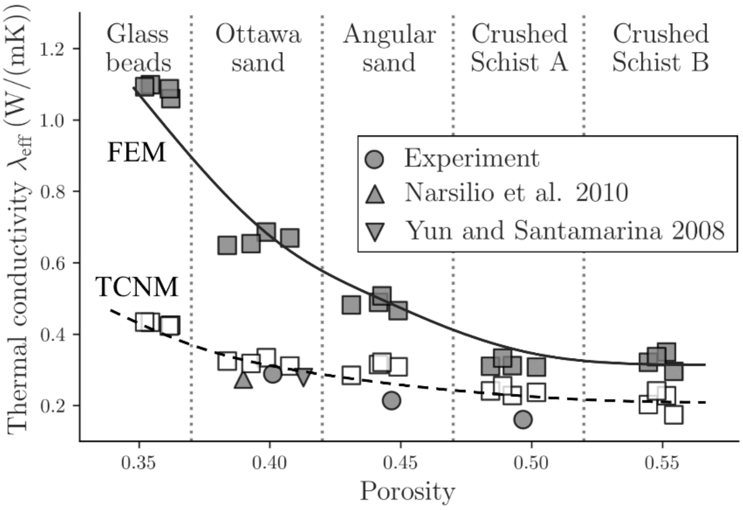

Fig. 11. The effective thermal conductivity calculated from TCNM compared with the finite element numerical and experimental results.

Fig. 11 illustrates that the λ_{eff} from TCNM shows good agreement with the experimental results, despite a slight overestimation of λ_{eff} for high-porosity samples. Woodside and Messmer [67] indicate that an underestimation may occur in the thermal needle test because of the imperfect contact between the needle and particles. Moreover, the mineralogy in the real materials is not considered in simulations. The effective thermal conductivity from TCNM shows a moderate decreasing rate with porosity. This observation is consistent with the results from papers [32, 34] that reported small decreases in effective thermal conductivity when porosity is increased without loading. In contrast, the λ_{eff} from FEM shows a much larger overestimation, which can be attributed to the oversmoothing of the interparticle contact area as shown in Fig. 7 since interparticle contact dominates the heat transfer in dry granular materials [1]. The FEM simulation also has limited ability to capture inter-particle contact surface roughness so that the actual point-to-point contacts in real imperfect particle-contacts are overestimated as flat face-to-face contacts [54, 68]. The overestimation of FEM is most obvious for samples with low porosity. For glass beads, the FEM value is almost three times the TCNM value. A higher porosity in granular materials usually means fewer interparticle contacts (coordination number in Fig. 12 (d)), resulting in the lower overestimation in FEM. Thus, FEM predicts the effective thermal conductivity more accurately in dense granular materials whereas TCNM may render accurate predictions for a wider range of materials.

4.2 Variation of λ_{eff} under loading: a particle-scale analysis

Another advantage of using TCNM to calculate λ_{eff}^{TCNM} is that the thermal conductances (Equations 4 and 6) between two particles can be readily computed at the microscale. Hence, the contribution of near-contact conductance (at the blue edges in Fig. 8) to the λ_{eff}^{TCNM} of a sample can be distinguished in the overall calculations by computing the difference of λ_{eff}^{TCNM} with and without near-contact conductance. Fig. 12 (a) shows the evolution of the average λ_{eff}^{TCNM} of the four subsamples of different materials under increasing loading. Round glass beads show the largest λ_{eff}^{TCNM} compared with the λ_{eff}^{TCNM} of the most irregular crushed schist B, which consistently showed the lowest conductivity among the four materials. Fig. 12 (b) shows that the contribution of the near-contact conductance to the λ_{eff}^{TCNM} is the lowest in round glass beads and highest in the schist B. Surprisingly, the contribution of the near-contact conductance is approximately 40% in crushed schist B with no compression. Even for the dense irregular sand (rounder than crushed schist B) under 10 MPa, the contribution still accounts for 25%. The contribution will be higher with the increase of gas pressure in dry granular materials with low porosity due to Smoluchowski effect (gas thermal conductivity reduces with the decreasing pressure) [69, 70]. The high contribution of the near-contact conductance is related to the number of near-contacts. As show in Fig. 3, two kinds of edges are created in a thermal network; one type of edge only considers the pure near-contact and the other involves both interparticle contact and near-contact. Indeed, Fig. 12 (c) shows that the percentage of the pure near-contact in the materials under any loading is larger than 50%. A higher number of near-contacts may indicate loose interparticle contacts. For instance, Angular sand has higher near-contact count than Ottawa sand, in Fig. 12 (c), but less interparticle contacts (as shown by coordination number in Fig. 12 (d)). Notably, the Ottawa sand has fewer near-contacts and real interparticle contacts than glass beads.

For the sensitivity of λ_{eff}^{TCNM} to the loading, the λ_{eff}^{TCNM} of the four materials increase substantially up to 2 MPa. During this loading period, the role of the near-contacts weakens in contrast with the higher contribution of interparticle contact number (coordination number) in Fig. 12 (d) and the interparticle contact quality (contact area) in Fig. 12 (e). When the load is increased, the λ_{eff}^{TCNM} remains steady for glass beads and slowly increases for Ottawa sand and angular sand. These trends are also observed in the variation of the coordination number but not in the change in the contact area. Hence, the interparticle contact number may be more important to heat transfer in granular materials than the near-contact and contact areas. Furthermore, the ordering of the materials in Fig. 11, Fig. 12 (a), Fig. 12 (b) and Fig. 12 (d) indicates that packings with more irregular particles could have higher porosity, lower interparticle contact [1, 71] and a resulting lower λ_{eff}^{TCNM}. The λ_{eff}^{TCNM} of crushed schist B reaches the same value as angular sand when the pressure is 6 MPa. The large increment of λ_{eff}^{TCNM} for crushed schist B is due to the particle breakage (Fig. 13), which isc indicated by the distinct decrease in its particle volume, shown in Fig. 12 (f). The earlier particle breakage in crushed schist B is because it contains a large proportion of biotite in the schist (Fig. 2) with lower Mohs hardness (2.5 - 3) than that of quartz (7) composing Ottawa sand [72]. Particles in crushed schist B with more irregular shape than the particles in Ottawa sand are more prone to breakage [73].

<Fig. 12 around here>

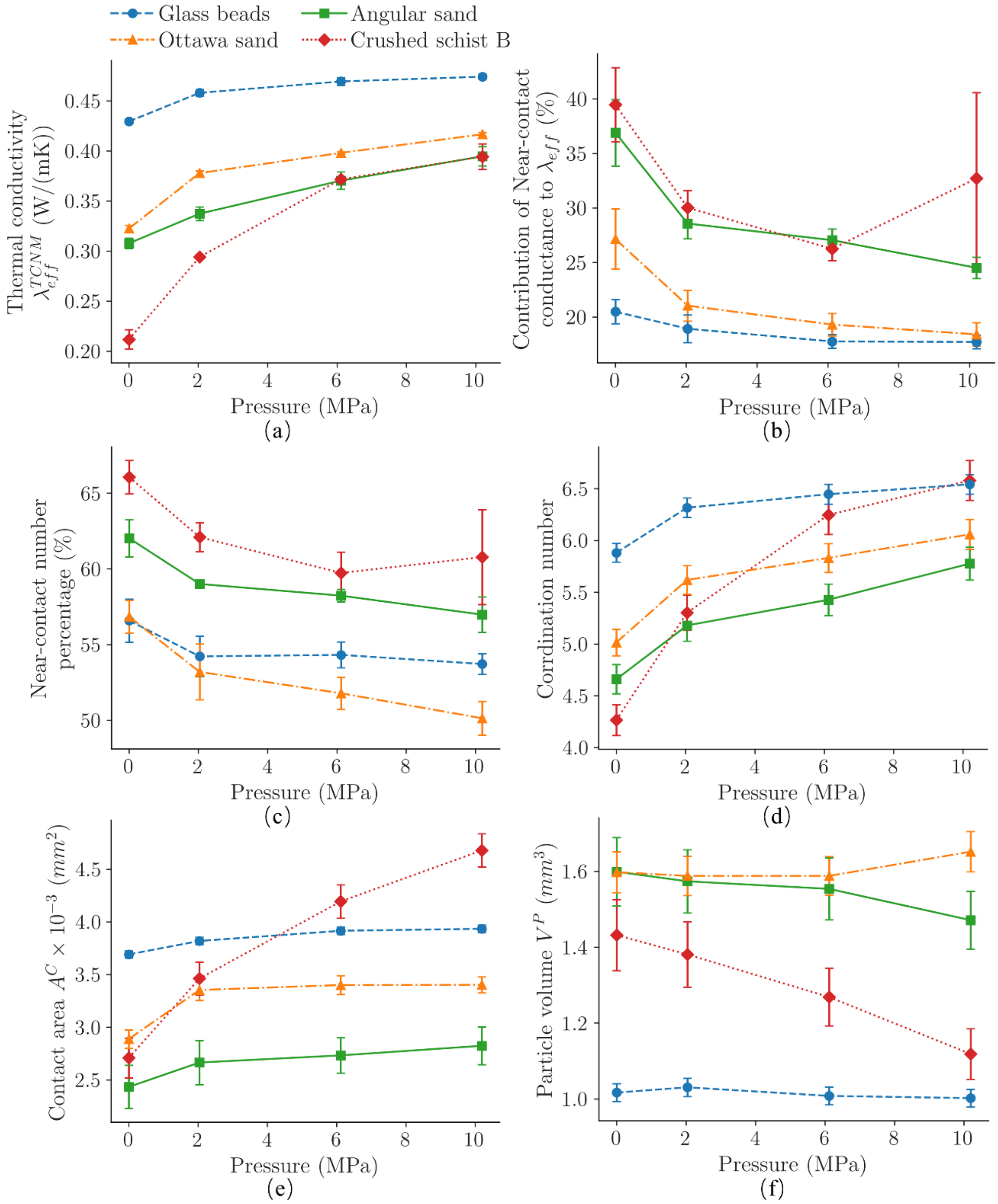

Fig. 12. Contribution of the near-contact conductance to λ_{eff}^{TCNM} and microstructural analysis of the near-contact percentage, coordination number, contact area and particle volume. For the thermal conductivity, contribution of near-contact and near-contact percentage, the error bar shows the range of the average from four subsamples for each material. For others, the error bar shows the 95% confidence interval calculated on network nodes or edges of the combined set of the four subsamples.

<Fig. 13 around here>

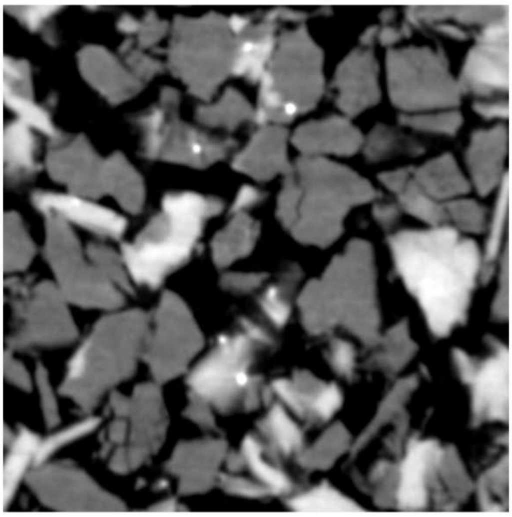

Fig. 13. Particle breakage in crushed schist B under 6 MPa.

4.3 Variation in λ_{eff} under loading: Rigidity and a multi-scale analysis

Although the variation in the coordination number in Fig. 12 (d) indicates the sensitivity of particle connectivity to compaction, the coordination number only describes the particle-scale rather than the mesoscale structure. Since particle connectivity changes due to the particle sedimentation and rotation during compression [40], N_3-cycles and clustering coefficients can make up for the disadvantage of using the coordination number to determine the change in the mesoscale structure and show the rigidity of the granular materials. We remind the readers that a 3-cycle is the smallest arrangement of particles formed by 3 neighbouring particles in contact, and that a higher count of 3-cycles structures than n-cycles (n>3) indicate higher rigidity of the overall assembly, i.e., a low count of 3-cycles indicates that the granular material is more deformable... Fig. 14 (a) shows that higher pressure results in a higher N_3-cycle number. The round glass beads have the most N_3-cycles among all materials at almost all levels of loading, which indicates that the regular particle packings are more rigid to the level of loading [74]. The continuously increasing number of N_3-cycles in crushed schist B is due to the decreasing particle volume, which means that the N_3-cycles reflect the particle breakage in Fig. 14 (b). The ordering of the global clustering coefficient for all materials at different levels is similar to that of N_3-cycles and its relationship with pressure in different materials become closer. Moreover, the local clustering coefficient in Fig. 14 (c) can almost unify the mesoscale structure change in the four granular materials under loading. Hence, it was used to further analyze the relationship between the rigidity and λ_{eff}^{TCNM} in dry granular materials.

<Fig. 14 around here>

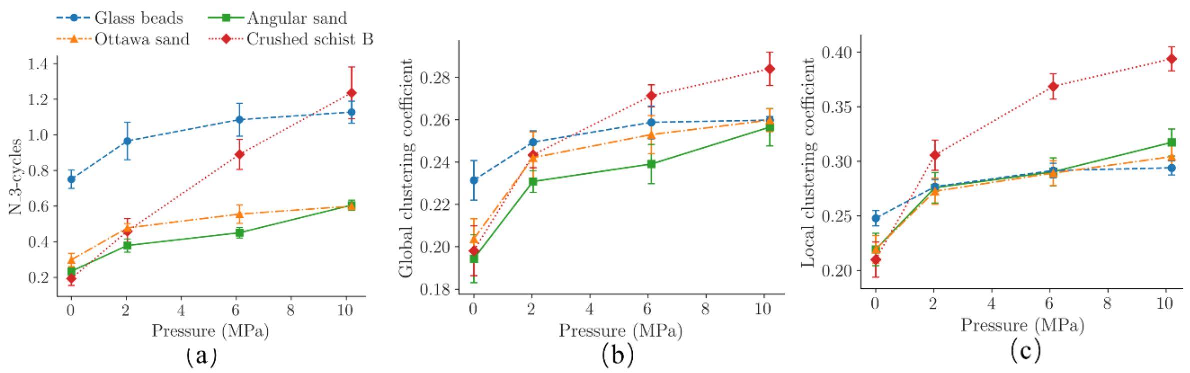

Fig. 14. Variation of mesoscale structural features under pressure. For N_3-cycles and global clustering coefficient, the error bar shows the range of the average from four subsamples for each material. For local clustering coefficient, the error bar shows the 95% confidence interval calculated on network nodes or edges of the combined set of the four subsamples.

Fig. 15 (a) shows that samples with a higher local clustering coefficient have a high normalized λ_{eff}^{TCNM}. Among the four materials, the range of the local clustering coefficient of round glass beads is narrow while that of the very irregular crushed schist sand is wide. Fig. 11As the local clustering coefficient quantifies the percentage of possible triangles through a node, the different range of the local clustering coefficient may because of the different particle shape. The decreasing range of the local clustering coefficient from irregular crushed schist B to round granular materials also reveals that samples with a regular particle shape are more rigid to loading. A linear regression was also conducted to fit the relationship for each material. The fitted lines for the four materials have a similar slope, from 0.29 in angular sand to 0.37 in Ottawa sand, which indicates that local clustering coefficient as a rigidity feature can capture the similar impacts of deformation on heat transfer in different materials. The relationship between the traditional porosity and normalized thermal conductivity is shown in Fig. 15 (b). The λ_{eff}^{TCNM} decreases linearly for each sample. However, the decreasing rates exhibit differences of 0.40 in crushed schist B and 0.73 in Ottawa sand. As local clustering coefficient measures the density of triangles, a material with a larger local clustering coefficient means that it has more "triangles" and is denser. Hence the porosity reduces with the increase of local clustering coefficient as shown in Fig. 15 (c).

<Fig. 15 around here>

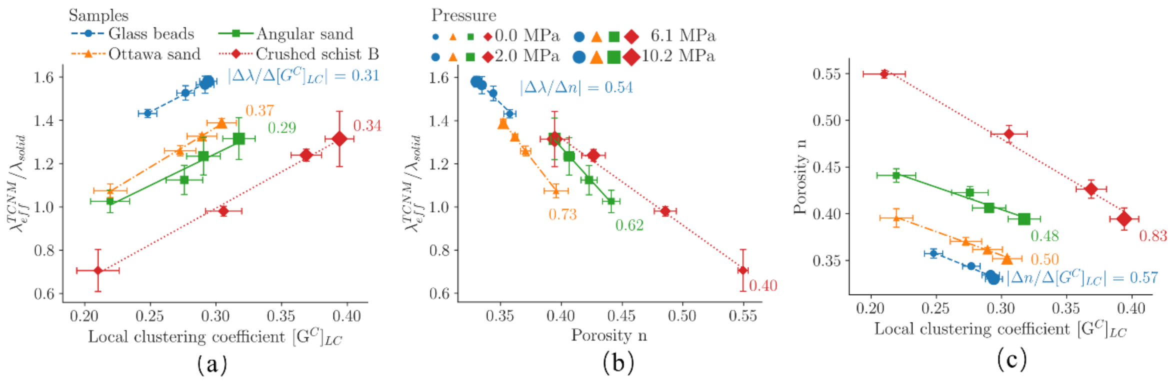

Fig. 15. The relationship between mesoscale local clustering coefficient, macroscale porosity and dimensionless λ_{eff}^{TCNM} calculated from TCNM. For thermal conductivity and porosity, the error bar

shows the range of the average from four subsamples for each material. For local clustering coefficient, the error bar shows the 95% confidence interval calculated on network nodes or edges of the combined set of the four subsamples.

Since particle shape affects the contact conductance and the observed importance in Fig. 15 (a), the average sphericity and roundness were employed to extend Fig. 15 (a) in three dimensions (Fig. 16 (a)). A plane also fits the relationship between the rigidity variable (local clustering coefficient), particle shape and λ_{eff}^{TCNM}. The results show that the correlation coefficient is high at 0.95, which indicates that a rigid structure variable with particle shape descritpors can be used to well predict the effective thermal conductivity of granular materials under deformation Although still high, the correlation coefficient decreases to 0.90 if the traditional porosity is considered as the controlling variable instead of the local clustering coefficient (Fig. 16 (b)). To show the robustness of TCNM and derived nonconventional features, the relationship between the two microstructural parameters and the λ_{eff}^{FEM} calculated using FEM is depicted in Fig. 16 (c). After the linear regression, the correlation between them is lower, 0.81. The higher correlation coefficient in Fig. 16 (b) is because TCNM values are closer to the experimental results as shown in Fig. 11.

<Fig. 16 around here>

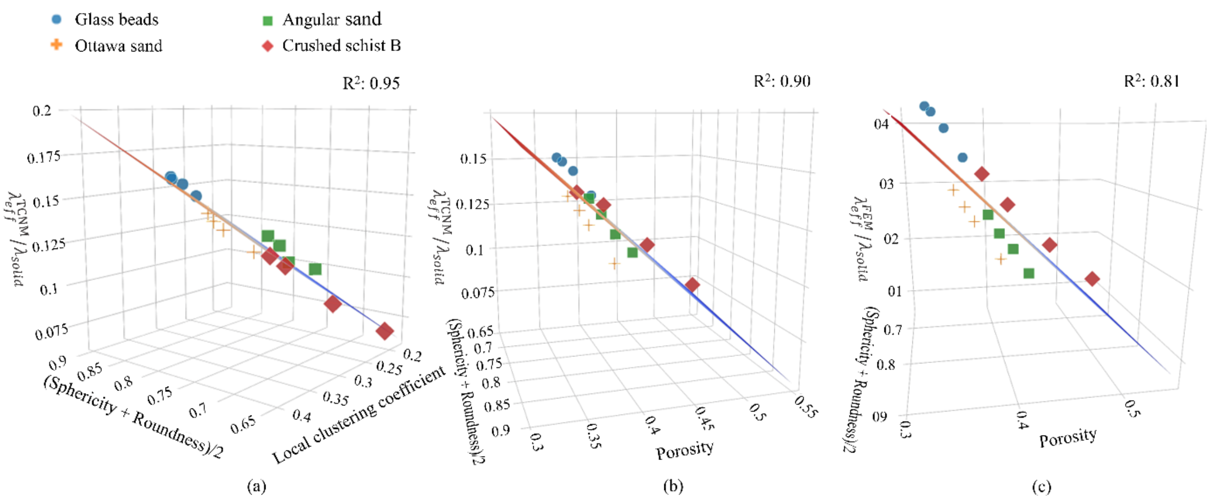

Fig. 16. The dimensionless λ_{eff}^{TCNM} shows a better relationship with particle shape and local clustering coefficient than with particle shape and porosity. (Click here to access the interactive graphs).

5 Conclusions

This work investigated the impact of microstructure variation on effective thermal conductivity. A thermal conductance network model (TCNM) was used to calculate the effective thermal conductivity λ_{eff} of granular materials based on CT images. By comparing the results with those from FEM and experimental measurements, the TCNM was found to be robust and without as much overestimation as FEM when calculating λ_{eff}. Since TCNM is derived from the thermal network by adding thermal conductance at network edges, it has another advantage over FEM in that the contribution of heat transfer from gaps and 'near-contacts' between particles can be identified. This work shows that this particular contribution is larger in irregular granular particles than in more rounded and regular particles at approximately 40% in crushed schist sand without loading. Additionally, three variables (3-cycle, global clustering coefficient and local clustering coefficient) from the contact network indicate the variation of the mesoscale structures of the granular packings under compaction. Comparing their variation in all samples with the increasing loading indicates that the local clustering coefficient may be best suited to quantify the 'rigidity' of granular materials. To make up for the shortcoming of the mesoscale rigidity parameter, which does not have a direct relation with the contact conductance, a microscale particle shape descriptor was calculated for each particle in the granular materials. The local clustering and particle shape show higher correlations with λ_{eff} (with a coefficient of correlation as high as 0.95) than the traditional porosities of the materials. Hence, a mesoscale rigidity variable with microsalce particle shape descriptors can capture the underlying mechanisms. They can also describe and be used to well predict λ_{eff} in granular materials at a variety of confinements.

Conflict of interest

The authors declared that there is no conflict of interest.

Acknowledgements

This research was undertaken in the Imaging and Medical Beam Line (IMBL) at the Australian Synchrotron, Victoria, Australia. The authors would like to acknowledge Dr Anton Maksimenko and the other beam scientists at Australian Synchrotron for their support during our experiments. The authors also thank Dr Tabassm Afshar and Dr Xiuxiu Miao for their support in collecting the CT images. The first author thanks The University of Melbourne for offering the Melbourne Research Scholarship.

References

[1] T.S. Yun, J.C. Santamarina, Fundamental study of thermal conduction in dry soils, Granular matter, 10(3) (2008) 197.

[2] U. El Shamy, O. De Leon, R. Wells, Discrete element method study on effect of shear-induced anisotropy on thermal conductivity of granular soils, International Journal of Geomechanics, 13(1) (2013) 57-64.

[3] Y. Asakuma, Y. Kanazawa, T. Yamamoto, Thermal radiation analysis of packed bed by a homogenization method, International Journal of Heat and Mass Transfer, 73 (2014) 97-102.

[4] C. Argento, D. Bouvard, Thermal conductivity of granular media, Powders & grains, (1993) 129-134.

[5] R. Askari, S.H. Hejazi, M. Sahimi, Thermal Conduction in Deforming Isotropic and Anisotropic Granular Porous Media with Rough Grain Surface, Transport in Porous Media, 124 (2018) 221-236.

[6] B. Aduda, Effective thermal conductivity of loose particulate systems, Journal of materials science, 31(24) (1996) 6441-6448.

[7] M. Gangadhara Rao, D. Singh, A generalized relationship to estimate thermal resistivity of soils, Canadian Geotechnical Journal, 36(4) (1999) 767-773.

[8] J. Côté, J.-M. Konrad, Thermal conductivity of base-course materials, Canadian Geotechnical Journal, 42(1) (2005) 61-78.

[9] L. Fletcher, Recent developments in contact conductance heat transfer, Journal of Heat Transfer, 110(4b) (1988) 1059-1070.

[10] Y. Hu, J. Wang, J. Yang, I. Mudawar, Q. Wang, Experimental study of forced convective heat transfer in grille-particle composite packed beds, International Journal of Heat and Mass Transfer, 129 (2019) 103-112.
[11] A. Tordesillas, Q. Lin, J. Zhang, R. Behringer, J. Shi, Structural stability and jamming of self-organized cluster conformations in dense granular materials, Journal of the Mechanics and Physics of Solids, 59(2) (2011) 265-296.
[12] L. Papadopoulos, M.A. Porter, K.E. Daniels, D.S. Bassett, Network analysis of particles and grains, Journal of Complex Networks, 6(4) (2018) 485-565.
[13] J. Scott, Social network analysis, Sociology, 22(1) (1988) 109-127.
[14] A.J. Liu, S.R. Nagel, W. Van Saarloos, M. Wyart, The jamming scenario-an introduction and outlook, in: Dynamical heterogeneities in glasses, colloids, and granular media, Oxford University Press, 2011.
[15] W. Dai, D. Hanaor, Y. Gan, The effects of packing structure on the effective thermal conductivity of granular media: A grain scale investigation, International Journal of Thermal Sciences, 142 (2019) 266-279.
[16] G. Fu, S. Wilkinson, R.J. Dawson, A spatial network model for civil infrastructure system development, Computer‐Aided Civil and Infrastructure Engineering, 31(9) (2016) 661-680.
[17] S. Argyroudis, J. Selva, P. Gehl, K. Pitilakis, Systemic seismic risk assessment of road networks considering interactions with the built environment, Computer‐Aided Civil and Infrastructure Engineering, 30(7) (2015) 524-540.
[18] A. Bozza, D. Asprone, F. Parisi, G. Manfredi, Alternative resilience indices for city ecosystems subjected to natural hazards, Computer‐Aided Civil and Infrastructure Engineering, 32(7) (2017) 527-545.
[19] H.M. Jaeger, T. Shinbrot, P.B. Umbanhowar, Does the granular matter?, Proceedings of the National Academy of Sciences, 97(24) (2000) 12959-12960.
[20] M.E. Newman, The structure and function of complex networks, SIAM review, 45(2) (2003) 167-256.
[21] J.H. van der Linden, G.A. Narsilio, A. Tordesillas, Machine learning framework for analysis of transport through complex networks in porous, granular media: a focus on permeability, Physical Review E, 94(2) (2016) 022904.
[22] A.G. Smart, J.M. Ottino, Evolving loop structure in gradually tilted two-dimensional granular packings, Physical Review E, 77(4) (2008) 041307.
[23] N. Rivier, Extended constraints, arches and soft modes in granular materials, Journal of non-crystalline solids, 352(42-49) (2006) 4505-4508.
[24] R.M. Baram, H. Herrmann, N. Rivier, Space-filling bearings in three dimensions, Physical review letters, 92(4) (2004) 044301.
[25] J. Kim, Y.-R. Goo, I. Choi, S. Kim, D. Lee, Toward high-accuracy and high-applicability of a practical model to predict effective thermal conductivity of particle-reinforced composites, International Journal of Heat and Mass Transfer, 131 (2019) 863-872.
[26] A.M. Abyzov, A.V. Goryunov, F.M. Shakhov, Effective thermal conductivity of disperse materials. I. Compliance of common models with experimental data, International Journal of Heat and Mass Transfer, 67 (2013) 752-767.
[27] F. Liu, Y. Cai, L. Wang, J. Zhao, Effects of nanoparticle shapes on laminar forced convective heat transfer in curved ducts using two-phase model, International Journal of Heat and Mass Transfer, 116 (2018) 292-305.
[28] W. Fei, G. Narsilio, M. Disfani, Impact of three-dimensional sphericity and roundness on heat transfer in granular materials (Under review), Powder Technology, (2019).
[29] A. Abbas, M.E. Kutay, H. Azari, R. Rasmussen, Three‐dimensional surface texture characterization of Portland cement concrete pavements, Computer‐Aided Civil and Infrastructure Engineering, 22(3) (2007) 197-209.
[30] M.E. Kutay, A.H. Aydilek, Pore pressure and viscous shear stress distribution due to water flow within asphalt pore structure, Computer‐Aided Civil and Infrastructure Engineering, 24(3) (2009) 212-224.

[31] M.R. Khelifa, S. Guessasma, New computational model based on finite element method to quantify damage evolution due to external sulfate attack on self‐compacting concretes, Computer‐Aided Civil and Infrastructure Engineering, 28(4) (2013) 260-272.
[32] G.A. Narsilio, J. Kress, T.S. Yun, Characterisation of conduction phenomena in soils at the particle-scale: Finite element analyses in conjunction with synthetic 3D imaging, Computers and Geotechnics, 37(7) (2010) 828-836.
[33] L. Miettinen, P. Kekäläinen, T. Turpeinen, J. Hyväluoma, J. Merikoski, J. Timonen, Dependence of thermal conductivity on structural parameters in porous samples, AIP Advances, 2(1) (2012) 012101.
[34] T.S. Yun, T.M. Evans, Three-dimensional random network model for thermal conductivity in particulate materials, Computers and Geotechnics, 37(7) (2010) 991-998.
[35] R.K. Desu, A.R. Peeketi, R.K. Annabattula, Artificial neural network-based prediction of effective thermal conductivity of a granular bed in a gaseous environment, Computational Particle Mechanics, 6(3) (2019) 503-514.
[36] O. Birkholz, Y. Gan, M. Kamlah, Modeling the effective conductivity of the solid and the pore phase in granular materials using resistor networks, Powder Technology, 351 (2019) 54-65.
[37] J.H. van der Linden, G. Narsilio, A. Tordesillas, Thermal conductance network model for computerised tomography images of real geomaterials (Under review), Computers and Geotechnics, (2019).
[38] ASTM, C778-17 standard specification for standard sand, ASTM International, West Conshohocken, PA, (2017).
[39] A. VandenBerg, The Tasman Fold Belt system in Victoria: geology and mineralisation of Proterozoic to Carboniferous rocks, Geological Survey of Victoria, 2000.
[40] T. Afshar, M. Disfani, G. Narsilio, A. Arulrajah, Changes to Grain Properties due to Breakage in a Sand Assembly using Synchrotron Tomography, in: EPJ Web of Conferences, EDP Sciences, 2017, pp. 07004.
[41] B. Persson, O. Albohr, U. Tartaglino, A. Volokitin, E. Tosatti, On the nature of surface roughness with application to contact mechanics, sealing, rubber friction and adhesion, Journal of physics: Condensed matter, 17(1) (2004) R1.
[42] M. Wiebicke, E. Andò, I. Herle, G. Viggiani, On the metrology of interparticle contacts in sand from x-ray tomography images, Measurement Science and Technology, 28(12) (2017) 124007.
[43] N. Otsu, A threshold selection method from gray-level histograms, IEEE transactions on systems, man, and cybernetics, 9(1) (1979) 62-66.
[44] S. Schlüter, A. Sheppard, K. Brown, D. Wildenschild, Image processing of multiphase images obtained via X‐ray microtomography: a review, Water Resources Research, 50(4) (2014) 3615-3639.
[45] Z. Karatza, E. Andò, S. Papanicolopulos, J. Ooi, G. Viggiani, Evolution of deformation and breakage in sand studied using X-ray tomography, Géotechnique, 1 (2018) 1-11.
[46] J. Schindelin, I. Arganda-Carreras, E. Frise, V. Kaynig, M. Longair, T. Pietzsch, S. Preibisch, C. Rueden, S. Saalfeld, B. Schmid, Fiji: an open-source platform for biological-image analysis, Nature methods, 9(7) (2012) 676.
[47] D. Legland, I. Arganda-Carreras, P. Andrey, MorphoLibJ: integrated library and plugins for mathematical morphology with ImageJ, Bioinformatics, 32(22) (2016) 3532-3534.
[48] H. Kim, C.T. Haas, A.F. Rauch, C. Browne, 3D image segmentation of aggregates from laser profiling, Computer‐Aided Civil and Infrastructure Engineering, 18(4) (2003) 254-263.
[49] H. Taylor, C. O'Sullivan, W. Sim, A new method to identify void constrictions in micro-CT images of sand, Computers and Geotechnics, 69 (2015) 279-290.
[50] J. Fonseca, C. O'Sullivan, M.R. Coop, P. Lee, Non-invasive characterization of particle morphology of natural sands, Soils and Foundations, 52(4) (2012) 712-722.
[51] D.J. Watts, S.H. Strogatz, Collective dynamics of 'small-world'networks, nature, 393(6684) (1998) 440.
[52] G.K. Batchelor, R. O'brien, Thermal or electrical conduction through a granular material, Proc. R. Soc. Lond. A, 355(1682) (1977) 313-333.
[53] M. Shapiro, V. Dudko, V. Royzen, Y. Krichevets, S. Lekhtmakher, V. Grozubinsky, M. Shapira, M. Brill, Characterization of Powder Beds by Thermal Conductivity: Effect of Gas Pressure on the

Thermal Resistance of Particle Contact Points, Particle & Particle Systems Characterization, 21(4) (2004) 268-275.

[54] R. Askari, S. Taheri, S.H. Hejazi, Thermal conductivity of granular porous media: A pore scale modeling approach, AIP Advances, 5(9) (2015).

[55] R. Bauer, E. Schlunder, Effective radial thermal-conductivity of packings in gas flow, part -ii: Thermal conductivity of packing fraction without gas flow, International Chemical Engineering, 18(2) (1978) 189-204.

[56] J.T. Gostick, Versatile and efficient pore network extraction method using marker-based watershed segmentation, Physical Review E, 96(2) (2017) 023307.

[57] J. Sundberg, P.-E. Back, L.O. Ericsson, J. Wrafter, Estimation of thermal conductivity and its spatial variability in igneous rocks from in situ density logging, International Journal of Rock Mechanics and Mining Sciences, 46(6) (2009) 1023-1028.

[58] G.A. Narsilio, O. Buzzi, S. Fityus, T.S. Yun, D.W. Smith, Upscaling of Navier–Stokes equations in porous media: Theoretical, numerical and experimental approach, Computers and Geotechnics, 36(7) (2009) 1200-1206.

[59] G. Narsilio, T. Yun, J. Kress, T. Evans, Hydraulic and thermal conduction phenomena in soils at the particle-scale: Towards realistic FEM simulations, in: IOP Conference Series: Materials Science and Engineering, IOP Publishing, 2010, pp. 012086.

[60] Simpleware Ltd., Simpleware ScanIP, http://www.simpleware.com/software/scanip, Date of access, 15 (2015) 12.

[61] COMSOL AB, COMSOL multiphysics v5.0, http://www.comsol.com, (2015).

[62] ASTM D5334-14, Standard Test Method for Determination of Thermal Conductivity of Soil and Soft Rock by Thermal Needle Probe Procedure, in, ASTM International, West Conshohocken, PA, 2014.

[63] T. Brandon, J. Mitchell, Factors influencing thermal resistivity of sands, Journal of Geotechnical Engineering, 115(12) (1990) 1683-1698.

[64] H. Wadell, Volume, shape, and roundness of rock particles, The Journal of Geology, 40(5) (1932) 443-451.

[65] G. Taubin, Curve and surface smoothing without shrinkage, in: Computer Vision, 1995. Proceedings., Fifth International Conference on, IEEE, 1995, pp. 852-857.

[66] B. Zhou, J. Wang, H. Wang, Three-dimensional sphericity, roundness and fractal dimension of sand particles, Géotechnique, 68(1) (2017) 18-30.

[67] W. Woodside, J. Messmer, Thermal conductivity of porous media. I. Unconsolidated sands, Journal of applied physics, 32(9) (1961) 1688-1699.

[68] G. Narsilio, T.S. Yun, J. Kress, T. Evans, Hydraulic and thermal conduction phenomena in soils at the particle-scale: Towards realistic FEM simulations, in: IOP Conference Series: Materials Science and Engineering, IOP Publishing, 2010, pp. 012086.

[69] M. Moscardini, Y. Gan, S. Pupeschi, M. Kamlah, Discrete element method for effective thermal conductivity of packed pebbles accounting for the Smoluchowski effect, Fusion Engineering and Design, 127 (2018) 192-201.

[70] W. Dai, S. Pupeschi, D. Hanaor, Y. Gan, Influence of gas pressure on the effective thermal conductivity of ceramic breeder pebble beds, Fusion Engineering and Design, 118 (2017) 45-51.

[71] J. Choo, Y.J. Kim, J.H. Lee, T.S. Yun, J. Lee, Y.S. Kim, Stress-induced evolution of anisotropic thermal conductivity of dry granular materials, Acta Geotechnica, 8(1) (2013) 91-106.

[72] J.W. Anthony, R.A. Bideaux, K.W. Bladh, M.C. Nichols, Handbook of mineralogy, Mineral Data Publ. Tucson, 1990.

[73] D. Wei, B. Zhao, D. Dias-da-Costa, Y. Gan, An FDEM study of particle breakage under rotational point loading, Engineering Fracture Mechanics, (2019).

[74] G.-C. Cho, J. Dodds, J.C. Santamarina, Particle shape effects on packing density, stiffness, and strength: natural and crushed sands, Journal of geotechnical and geoenvironmental engineering, 132(5) (2006) 591-602.

List of Tables

List of Figures